RSC Advances

PAPER

Check for updates

Cite this: *RSC Adv.*, 2022, **12**, 11722

# The crystal structures, phase stabilities, electronic structures and bonding features of iridium borides from first-principles calculations†

Jinquan Zhang,[a] Yuanyuan Jin,*[a] Chuanzhao Zhang,*[a] Yanqi Wang,[a] Libiao Tang,[a] Song Li,[a] Meng Ju,[b] Jingjing Wang,[c] Weiguo Sun[d] and Xilong Dou[e]

We present results of an unbiased structure search for the lowest energy crystalline structures of various stoichiometric iridium borides, using first-principles calculations combined with particle swarm optimization algorithms. As a result, besides three stable phases of *C*2/*m*-$Ir_3B_2$, *Fmm*2-$Ir_4B_3$, and *Cm*-$Ir_4B_5$, three promising metastable phases, namely, $P2_1/m$-$Ir_2B$, $P2_1/m$-IrB, and *Pnma*-$Ir_3B_4$, whose energies are within 20 meV per atom above the convex hull curve, are also identified at ambient pressure. The high bulk modulus of 301 GPa, highest shear modulus of 148 GPa, and smallest Poisson's ratio of 0.29 for *C*2/*m*-$Ir_3B_2$ make it a promising low compressible material. *C*2/*m*-$Ir_3B_2$ is predicted to possess the highest Vickers hardnesses, with a Vickers hardness of 13.1 GPa and 19.4 GPa based on Chen's model and Mazhnik-Oganov's model respectively, and a high fracture toughness of 5.17 MPa $m^{0.5}$. The anisotropic indexes and the three-dimensional surface constructions of Young's modulus indicate that Ir–B compounds are anisotropic with the sequence of the elastic anisotropy of $Ir_2B$ > IrB > $Ir_4B_5$ > $Ir_3B_4$ > $Ir_4B_3$ > $Ir_3B_2$. Remarkably, these iridium borides are all ductile. We further find that the four Ir–B phases of $P2_1/m$-$Ir_2B$, *C*2/*m*-$Ir_3B_2$, $P2_1/m$-IrB, and *Fmm*2-$Ir_4B_3$ possess dominant Ir–B covalent bonding character, while strong B–B and Ir–B covalent bonds are present in *Cm*-$Ir_4B_5$ and *Pnma*-$Ir_3B_4$, which are responsible for their excellent mechanical properties.

Received 11th March 2022
Accepted 8th April 2022

DOI: 10.1039/d2ra01593e

rsc.li/rsc-advances

## 1 Introduction

With increasing demands for hard materials in industrial applications and the strict requirements in complex environments, transition metal borides have become the most important industrial materials because of their excellent wear resistance, ultra-incompressibility, high hardness, and high melting point.[1–8] Previous experimental studies have shown that many transition metal borides such as $ReB_2$ (ref. 9) (48 GPa), $OsB_2$ (ref. 10) (35.2 GPa), $CrB_4$ (ref. 11) (48 GPa), $WB_4$ (ref. 12) (43.3 GPa), and $MnB_4$ (ref. 13) (37.4 GPa) have high hardness and can be synthesized under normal or low relative pressure through arc melting, making their production cost lower and easier to expand. Notably, the combination of structure searching algorithms with first principles calculations, play a key role in understanding the origin of high hardness and in accelerating the discovery of some hard materials.[14–18]

Crystal structure search has been widely applied to predict binary hard and superhard materials (*i.e.* compounds with Vickers hardness > 40 GPa) because it can search for a series of stable and metastable phases only with given components, which provides a powerful tool for the systematic exploration of binary transition metal borides.[19] Therefore, previous researchers have systematically studied many binary transition metal borides by using structure search to find some borides with high hardness and fully understand the thermodynamic properties of the system.[20–25] Although previous researchers have done a lot of research on the Y–B binary system for a long time, Ding *et al.* used CALYPSO to systematically study Y–B system and found a new stable phase $R\bar{3}m$-$YB_6$ with the hardness of about 37 GPa. Besides, they also found that the previously high-temperature synthesized $YB_4$ is in metastable phase in the Y–B system.[21] In addition, the systematic study of the compounds can also guide subsequent experiments and solve the uncertainty of boride structure caused by the difficulty in determining the position of lighter boron atoms in experiments. For example, A. N. Kolmogorov *et al.* have systematically studied the Fe–B system[20] and found that the orthogonal

[a]*Department of Physics and Optoelectronic Engineering, Yangtze University, Jingzhou 434023, China. E-mail: scujyy@163.com; zcz19870517@163.com*

[b]*School of Physical Science and Technology, Southwest University, Chongqing 400715, China*

[c]*College of Computer and Information Engineering, Hubei Normal University, Huangshi 435002, China*

[d]*College of Physics and Electronic Information, Luoyang Normal University, Luoyang 471022, China*

[e]*Institute of Atomic and Molecular Physics, Sichuan University, Chengdu 610065, China*

† Electronic supplementary information (ESI) available. See https://doi.org/10.1039/d2ra01593e

This article is licensed under a Creative Commons Attribution-NonCommercial 3.0 Unported Licence.



© 2022 The Author(s). Published by the Royal Society of Chemistry

structure oP10-$FeB_4$ is metastable above the convex hull curve, which indicates that this compound may be stable at finite temperature. Subsequent high-temperature experiments show that orthogonal phase $FeB_4$ is a potential superconductor and superhard material, and its hardness is 43–70 GPa.[26] Recent theoretical studies using USPEX, a global crystal structure search technique, have systematically studied the W–B system and have predicted a new stable compound, superhard tungsten pentaboride $WB_5$, suggesting that the long-debated "$WB_4$" and the newly predicted $WB_5$ are actually the same material.[16,24] This finding better resolves the previous controversy over the structure of $WB_4$. Ir and Os are neighboring 5d transition metals in the periodic table and both have similar electronegativity, so Ir–B compounds were also considered as potential high hardness materials after the discovery of superhard $OsB_2$. Although previous theoretical and experimental studies have been carried out on the Ir–B system, the data on electronic properties and metastable phases of Ir–B compounds are quite limited, especially those close to convex hull curves of iridium boride, which may still have some problems in the study of metastable phases synthesized at high temperature.

For Ir–B system, iridium boride films with fractional stoichiometric ratios have attracted much attention due to their super-hard properties. Recently, iridium borides have attracted much attention because it is reported that $IrB_{1.35}$ has Vickers hardness of 49.8–18.2 GPa under a load of 0.49 and 9.81 N, respectively, which is potential superhard material.[27] Later, $IrB_{1.1}$ film (0.4 μm) was deposited on a silicon dioxide substrate by pulse deposition technology, with Vickers hardness as high as 43 GPa.[28] Subsequently, Zeilinger *et al.*[22] and Wang *et al.*[23] systematically studied the Ir–B phase diagram and the mechanical properties of the stable phase on the convex hull curve. In 2016, two groups successfully used a mechanochemical approach to synthesize two new iridium borides, namely, $IrB_2$ and IrB, and found that IrB and $IrB_2$ ceramic nanopowders may be an active catalyst material.[29,30] However, these two newly discovered borides have been proved to be metastable phases close to the convex hull curve. Previous systematic studies and synthesis of many metastable phases in Ir–B system have fully demonstrated that the study of metastable phases in Ir–B systems is very important. These metastable phases can usually be synthesized by selecting suitable precursors and controlling the quenching rate. However, no independent search for potential metastable structures of Ir–B system beyond known structure types has been performed to date, and there has been no systematic study of their mechanical properties, elastic anisotropy, bonding nature, and hardness. The goal of this work is to address these deficiency.

To find stable and metastable compounds that may not have been previously observed experimentally or computationally, we performed here an extensive study on binary iridium borides using the Crystal Structure Analysis by Particle Swarm Optimization (CALYPSO)[31,32] method in combination with first-principles calculations. Finally, we reproduce the previously reported three stable structures and find three metastable structures that may be synthesized at high temperature, and comprehensively explore the structural characteristics and intrinsic physical properties of these structures from the microscopic level.

## 2 Computational methods

To comprehensively search for the stable and metastable structures in the Ir–B binary system under atmospheric pressure, our structure-searching simulations are based on a particle swarm optimization algorithm in conjunction with *ab initio* total-energy calculations, as conducted in CALYPSO code.[31,32] The significant feature of this code is that it can quickly predict the most stable and metastable 2D and 3D solid-state structures only requiring chemical compositions of a given compound at given external conditions and the superior efficiency of this methodology has been verified on various systems, spanning from elements to binary and ternary compounds.[33–37] Our structural searches with system sizes containing 1–6 formula units (f.u.) per simulation cell were performed for stoichiometries $Ir_mB_n$ varying from $Ir_3B$ to $IrB_3$.

All the following structural relaxations and electronic structure calculations were carried out with the utilization of density functional theory within the Perdew–Burke–Ernzerhof (PBE) exchange–correlation functional as implemented in the Vienna *ab initio* simulation package (VASP).[38,39] The electron–ion interaction was described *via* a projector augmented wave (PAW) potentials with $5d^76s^2$ and $2s^22p^1$ valence electron for Ir and B, respectively.[40] A plane wave cutoff energy of 600 eV and proper Monkhorst–Pack *k*-meshes were selected to guarantee that all the enthalpy calculations were well converged to better than 1 meV per atom.[41–43] To probe into the dynamical stability of $Ir_mB_n$ compositions, the phonon dispersion curves were calculated through the direct supercell approach as implemented in the Phonopy code.[44] In addition, the electron localization function (ELF)[45] and Bader charge[46] were also computed within the VASP code. To analyze the interatomic interaction and chemical bonding, the crystal orbital Hamilton populations (COHP) were calculated using the LOBSTER.[47] The independent single-crystal elastic constants could be ascertained on the basis of the stress tensor generated by employing a small strain to an optimized unit cell. Furthermore, the bulk modulus ($B$), shear modulus ($G$), Young's modulus ($E$), and Poisson's ratio ($\nu$) were thus determined by the Voigt–Reuss–Hill (VRH) approximation.[48] Vickers hardness was estimated according to the Chen[49] ($H_v^C$ (GPa)) and Mazhnik-Oganov[50] ($H_v^{MO}$ (GPa)) models. Fracture toughness was calculated using the empirical Mazhnik-Oganov model ($K_{IC}$).

Finally, for the purpose of fully describing the elastic anisotropy behavior of the considered structure in the Ir–B binary system, we constructed the three-dimensional model of Young's modulus by using the elastic anisotropy measurement (ElasticPOST) program.[51]

## 3 Results and discussion

### 3.1 Crystal structures and stability

To determine the stable and metastable phases of Ir–B compounds at ambient pressure, we have implemented

© 2022 The Author(s). Published by the Royal Society of Chemistry

structure searches using the CALYPSO method on iridium borides with various $Ir_mB_n$ compositions at considered pressures of 1 atm. This crystal structure search successfully reproduces the experimental structures of *Pnma*-IrB and $P6_3/mmc$-$IrB_2$ as the lowest ground state energy phases and the other theoretical ground phases of $C2/m$-$Ir_3B_2$, *Fmm*2-$Ir_4B_3$, and *Cm*-$Ir_4B_5$, thus providing important support for the reliability of the present structure searches.[22,23,29] Negative formation enthalpy shows that the synthesis of the substance through the reference phase is an exothermic process, and the exothermic reaction is easy to occur in nature. The formation enthalpies can be calculated with the following equation:

$$\Delta H = \frac{E(\mathrm{Ir}_x\mathrm{B}_y) - xE(\mathrm{Ir}) - yE(\mathrm{B})}{x+y} \quad (1)$$

Herein, $\Delta H$ is the formation enthalpy per atom for a compound of this stoichiometry, $E$(IrxBy) is the total energy per formula unit of the compound, and $E$(Ir) and $E$(B) represent the Ir and B ground states with the cubic phase[52] (space group: $Fm\bar{3}m$) and α-rhombohedral strcutue,[53] respectively. Subsequently, we use the formation enthalpy to evaluate the thermodynamic stability of iridium borides. The calculated lattice parameters, cell volume, total energy and formation enthalpy for the lowest energy structures and the selected metastable structures of each considered stoichiometry of the Ir–B system are tabulated in Table 1, in company with the previously experimental and theoretical results. On the basis of the formation enthalpies, the convex hull of the Ir–B binary system under atmospheric pressure is constructed as displayed in Fig. 1. The whole structural information for the lowest energy phases of each component considered in the binary Ir–B system under ambient pressure is listed in Table S1 of the ESI.† The

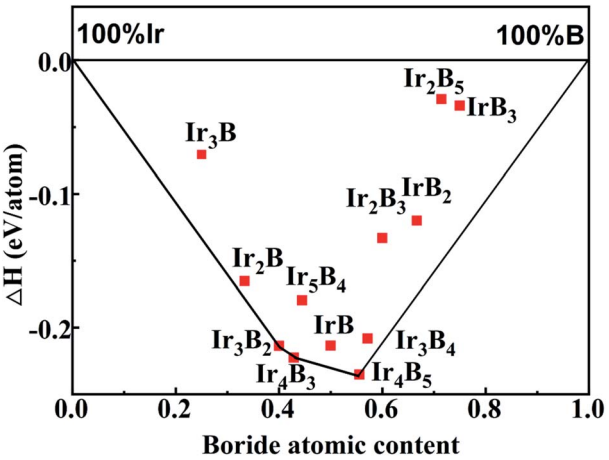


Fig. 1 The predicted formation enthalpy with respect to solid Ir and B for various Ir–B stoichiometries under atmospheric pressure. The solid line represents the ground state convex hull.

convex hull of these points then connects the structures with the lowest formation enthalpies among all stoichiometries, and any structures exactly located on the convex hull are deemed as energetically stable, both against decomposition into other elements or any combination of other binary phases, and thus experimentally synthetic. Furthermore, it should be specially pointed out that vibration effects may modify the convex hull curve at high temperatures, bringing out some structures that slightly deviate from the convex hull and approach to the convex hull. Therefore, it is extremely important to probe into not only the stable phases on the convex hull in Fig. 1, but also the metastable phases close to the convex hull curve. As presented in Fig. 1, it is obviously

Table 1 Calculated lattice parameters, *a*-axis, *b*-axis and *c*-axis (Å), cell volume *V* (Å$^3$), the total energy (eV per atom), and formation enthalpies per atom $\Delta H$ (eV per atom) for the relevant structures of various components of Ir–B system under ambient pressure, compared with experimental and theoretical consequences

| Phase | Space group | *a* (Å) | *b* (Å) | *c* (Å) | *V* (Å$^3$) | Total energy | $\Delta H$ |
|---|---|---|---|---|---|---|---|
| $Ir_3B$ | $P\bar{6}m2$ | 2.794 | 2.794 | 7.512 | 50.776 | −8.386 | −0.073 |
| $Ir_2B$ | $P2_1/m$ | 5.699 | 2.803 | 4.736 | 74.600 | −8.297 | −0.163 |
| | *Cmcm*[22] | 2.783 | 4.833 | 10.764 | 144.777 | −8.278 | −0.143 |
| $Ir_3B_2$ | $C2/m$ | 7.500 | 2.860 | 8.605 | 119.573 | −8.205 | −0.214 |
| $Ir_4B_3$ | *Fmm*2 | 5.659 | 5.731 | 10.020 | 324.942 | −8.154 | −0.224 |
| $Ir_5B_4$ | $P6_3/mmc$ | 3.521 | 3.521 | 18.957 | 203.535 | −8.077 | −0.181 |
| IrB | $P2_1/m$ | 6.723 | 3.926 | 3.555 | 92.714 | −7.990 | −0.214 |
| | *Pnma*[29] | 4.421 | 2.863 | 7.026 | 88.927 | −7.990 | −0.214 |
| | *Cmcm* | 4.036 | 5.850 | 3.926 | 92.694 | −7.990 | −0.213 |
| | $P\bar{6}m2$[22] | 3.051 | 3.051 | 2.713 | 21.876 | −7.966 | −0.190 |
| $Ir_4B_5$ | *Cm* | 10.623 | 2.902 | 12.373 | 189.252 | −7.894 | −0.236 |
| $Ir_3B_4$ | *Pnma* | 16.266 | 2.962 | 6.028 | 290.436 | −7.832 | −0.208 |
| $Ir_2B_3$ | $P6_3/mmc$ | 3.124 | 3.124 | 12.184 | 102.992 | −7.695 | −0.132 |
| $IrB_2$ | $C2/m$ | 7.422 | 2.856 | 5.898 | 115.360 | −7.544 | −0.125 |
| | *Pnma* | 3.151 | 4.543 | 4.040 | 57.825 | −7.540 | −0.121 |
| | *Pmmn*[56] | 5.586 | 2.983 | 6.818 | 113.619 | −7.515 | −0.095 |
| | $P6_3/mmc$[29] | 3.075 | 3.075 | 7.054 | 57.767 | −7.471 | −0.052 |
| $Ir_2B_5$ | $R3m$ | 2.976 | 2.976 | 24.747 | 189.793 | −7.347 | −0.030 |
| $IrB_3$ | *Pnma*[22] | 2.923 | 2.923 | 4.652 | 34.417 | −7.275 | −0.034 |
| | $P\bar{6}m2$ | 9.875 | 3.126 | 4.571 | 141.075 | −7.242 | −0.001 |


© 2022 The Author(s). Published by the Royal Society of Chemistry

found that the convex hull of Ir–B binary system contains three stable phases indicated as $Ir_3B_2$ ($C2/m$), $Ir_4B_5$ ($Fmm2$), and $Ir_4B_5$ ($Cm$). Besides the stable structures on the convex hull, three metastable phases, $Ir_2B$ ($P2_1/m$), IrB ($P2_1/m$), and $Ir_3B_4$ ($Pnma$), are very close to the convex hull curve, whose energies are 15 meV per atom, 17 meV per atom and 16 meV per atom above the convex hull curve, respectively. These three metastable phases near the convex hull curve were discovered for the first time and may be synthesized at high temperature.[25] We below focus on the structural, mechanical and anisotropy, and electronic properties, bonding characters and hardness for these six considered crystals.

Starting from the phase with low boron content, each phase is discussed separately. For $Ir_2B$, the orthogonal $Cmcm$ phase is considered to be the ground state phase by previous theory. By our method, we have reconstructed the orthogonal $Cmcm$ phase well.[23] Interestingly, our present calculations uncover a new crystal $P2_1/m$-$Ir_2B$, which is 0.019 eV per atom lower than the former. From Fig. 2a, each B atom is bonded with six Ir atoms, forming a trigonal prism ($Ir_6B$). By stacking the $Ir_6B$ building blocks in the way of sharing one edge of the trigonal prism, the trigonal-prism chain is constructed. In the connected $Ir_6B$ triangular prism, the Ir–B bond lengths vary between 2.14 and 2.20 Å, which is close to the strong covalent Ir–B bond of $P6_3/mmc$-$IrB_4$ (ref. 54) (2.189 Å), stating that there exists a strong covalent bond between Ir and B in $P2_1/m$-$Ir_2B$. Furthermore, the distance of the nearest B–B bonds is 4.6 Å, showing that there is no B–B interaction. For the stable $C2/m$-$Ir_3B_2$ polycrystal (see Fig. 2b), there are two layers of iridium atoms along the $c$-axis sandwiched with a double layer of graphite-like Ir/B rings. In the connected bilayer graphite-like Ir/B rings, the Ir–B distances range from 2.15 Å to 2.19 Å are close to that of the potential hard materials m-$IrB_2$ (2.18 Å) with a theoretical Vickers hardness of 13.82 GPa.[55]

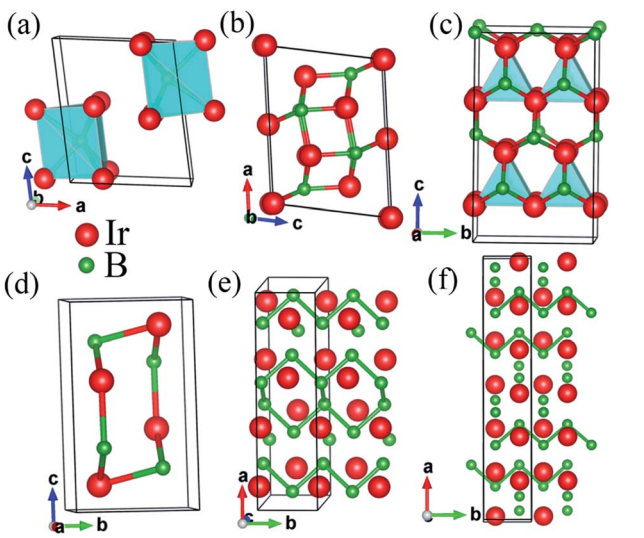


Fig. 2 Crystal structures of the six considered polymorps at ambient pressure. (a) $P2_1/m$-$Ir_2B$, (b) $C2/m$-$Ir_3B_2$, (c) $Fmm2$-$Ir_4B_3$ (d) $P2_1/m$-IrB, (e) $Cm$-$Ir_4B_5$ and (f) $Pnma$-$Ir_3B_4$. The red and green spheres represent the Ir and B atoms, respectively.

As shown in Fig. 2c, it is worth noting that the $Fmm2$-$Ir_4B_3$ structure has an alternating layered arrangement structure of B–Ir–B–Ir along the $c$-axis, and the layers are connected by $Ir_6B$ prism building blocks. In the alternating B–Ir–B–Ir layers, the distances between the nearest Ir–B bonds are all less than the sum (2.25 Å) of covalent radii of the B atom ($r$B = 0.84 Å) and Ir atom ($r$Ir = 1.41 Å). In particular, the minimum distance between B–B bonds is 4.03 Å, which is much larger than the possible bonding distance.

Subsequently, for IrB with a stoichiometric ratio of 1 : 1, previous theoretical calculations report three thermodynamically stable structures ($Pnma$,[56] $Cmcm$,[22] and $P\bar{6}m2$ (ref. 23)). Intriguingly, the present calculations uncover a novel ground state phase $P2_{11}/m$-IrB, whose formation enthalpy is about 0.024 eV per atom lower than that of the $P\bar{6}m2$-IrB phase, as summarized in Table 1. Surprisingly, the formation enthalpy of the $P2_1/m$-IrB structure is closely equal to that of $Pnma$-IrB synthesized in the above experiments at ambient pressure or $Cmcm$-IrB. As displayed in Fig. 2d, the $P2_1/m$-IrB crystal is composed of the twisted eight-membered ring formed by the alternating connection of Ir and B atoms. In an eight-membered ring, the maximum distance of Ir–B on the eight sides is 2.17 Å, and the minimum distance is 2.11 Å. The average Ir–B bond length of the $P2_1/m$-IrB is smaller than Ir–B (2.16 Å) covalent bonds in the $Pnma$-IrB under ambient pressure, indicating relatively strong Ir–B interactions.

At 1 < B/Ir < 2, the 1D B-ribbons are adopted by the lowest-energy structures of $Cm$-$Ir_4B_5$ and the metastable structure of $Pnma$-$Ir_3B_4$ at zero temperature, as shown in Fig. 2e and f. The distances between B–B bonds are respectively 2.00 Å and 2.02 Å in the 1D B-ribbons, which are very close to that of the potential hard materials $C2/m$-$VB_3$ of B–B bond distance (1.764–1.912 Å), indicating the existence of a strong B–B bond.[57] Besides the 1D B-ribbons, we also found the graphene-like B-sheet with short sides of 1.89 Å and long sides of 2.00 Å in $Cm$-$Ir_4B_5$, which is shorter than the high-pressure synthesis of β-$Ir_4B_5$ (2.122 Å).[58]

In general, it is worth noting that the distances of the nearest neighbor Ir–B bonds in these six considered structures are all smaller than the sum (2.25 Å) of the covalent radii of the B atom ($r$B = 0.84 Å) and the Ir atom ($r$Ir = 1.41 Å), demonstrating the strong covalent bonding between Ir and B in these six considered phases. However, with increasing B concentration, the number of Ir–B covalent bonds decreases, and strong B–B covalent bonds gradually appear for borides with 1 < B/Ir < 2.

As we all know, a crystal is dynamically stable if its potential energy always increases against any combinations of atomic displacements in the equilibrium state, which is given by: $\frac{\partial \Phi}{\partial r_\alpha(lk)} = 0$. In other words, this is equivalent to the condition that all phonons have real and positive frequencies. Phonons reflect the quantized properties of lattice vibration energy, which can be measured by phonon dispersion curve and phonon density of states.[59–62] Therefore, to clarify the dynamical stabilities of these six considered phases, their phonon spectra and phonon density of states were also calculated, as depicted in Fig. 3. From Fig. 3, it can be obviously found that there are no virtual phonon frequencies in the entire Brillouin zone, which

© 2022 The Author(s). Published by the Royal Society of Chemistry

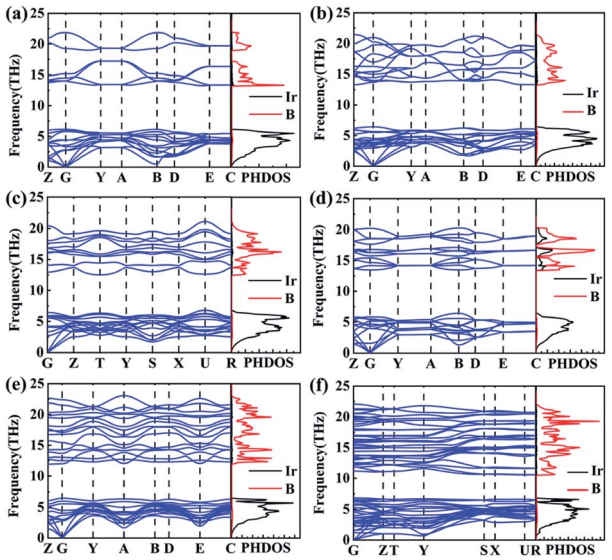


Fig. 3 Calculated phonon dispersion curves and projected phonon density of states (PDOS) of (a) $P2_1/m$-$Ir_2B$, (b) $C2/m$-$Ir_3B_2$, (c) $Fmm2$-$Ir_4B_3$ (d) $P2_1/m$-IrB, (e) $Cm$-$Ir_4B_5$ and (f) $Pnma$-$Ir_3B_4$ at ambient pressure.

proves that these six considered crystals are dynamically stable under environmental pressure. Moreover, the phonon bands for these six considered phases can be divided into two independent regions: the high-frequency mode mainly corresponds to the vibration of the boron atoms, while the low-frequency region is mainly related to the vibration of iridium atoms. This phenomenon stems from the larger atomic mass of the iridium atom than that of the boron atom.

### 3.2 Mechanical stabilities, mechanical properties and hardness

Elastic properties (such as elastic constants, elastic modulus, *etc.*) are essential for us to understand the deformation behavior of solids under the action of external forces, and can provide a deeper understanding of the macroscopic mechanical behavior, which is helpful to evaluate the mechanical properties of materials. The elastic constants of six considered phases were computed from the strain–stress method, along with previous results, which are collected in Table 2. The obtained elastic constants of $C2/m$-$Ir_3B_2$, $Fmm2$-$Ir_4B_3$ and $Cm$-$Ir_4B_5$ in Table 2, as well as the calculated bulk modulus, $B$, shear modulus, $G$, and Young's modulus, $E$, as listed in Table 3, are in good agreement with other available theoretical results, suggesting that the calculations in the present work are reasonable.[22,23]

In addition, the mechanical stability of a crystal can be assessed through elastic constants. As summarized in Table 2, all the six considered phases meet the respectively mechanical stability criterion, suggesting the mechanical stabilities for these six considered structures under ambient pressure. Moreover, the $C_{11}$, $C_{22}$, and $C_{33}$ values of six crystals (except $P2_1/m$-IrB) can be compared with that of the potential superhard material $TiB_2$ (39.6 GPa),[63] which implies that these five substances have larger incompressibility along the *a*-, *b*-, and *c*-axes. In general, the

Table 2 Calculated elastic constants $C_{ij}$ (GPa) for the six considered structures in the Ir–B binary system

| Phase | Space group | $C_{11}$ | $C_{22}$ | $C_{33}$ | $C_{44}$ | $C_{55}$ | $C_{66}$ | $C_{12}$ | $C_{13}$ | $C_{23}$ |
|---|---|---|---|---|---|---|---|---|---|---|
| $Ir_2B$ | $P2_1/m$ | 522 | 540 | 516 | 169 | 46 | 68 | 150 | 143 | 198 |
| $Ir_3B_2$ | $C2/m$ | 475 | 490 | 481 | 174 | 184 | 130 | 206 | 249 | 180 |
| $Ir_3B_2$ | $C2/m$[22] | 479 | 507 | 479 | 128 | 171 | 200 | 202 | 248 | 180 |
| $Ir_4B_3$ | $Fmm2$ | 473 | 603 | 456 | 90 | 93 | 119 | 176 | 199 | 228 |
| $Ir_4B_3$ | $Fmm2$ (ref. 22) | 486 | 655 | 473 | 96 | 101 | 112 | 165 | 215 | 185 |
| IrB | $P2_1/m$ | 291 | 297 | 338 | 139 | 123 | 103 | 127 | 218 | 163 |
| $P_1$-IrB | $Pnma$[56] | 514 | 368 | 438 | 55 | 227 | 106 | 108 | 333 | 183 |
| $Ir_4B_5$ | $Cm$ | 474 | 424 | 518 | 88 | 167 | 76 | 161 | 216 | 158 |
| $Ir_4B_5$ | $Cm$[23] | 494 | 438 | 514 | 85 | 104 | 166 | 131 | 213 | 153 |
| $Ir_4B_5$ | $Cm$[16] | 519 | 459 | 548 | 112 | 178 | 88 | 150 | 218 | 177 |
| α-$Ir_4B_5$ | $C2/m$[58] | 373 | 303 | 303 | 50 | 125 | 58 | 150 | 160 | 217 |
| β-$Ir_4B_5$ | $Pnma$[58] | 482 | 390 | 433 | 112 | 102 | 60 | 170 | 122 | 250 |
| $Ir_3B_4$ | $Pnma$ | 577 | 419 | 588 | 75 | 148 | 76 | 130 | 168 | 232 |
| $IrB_2$ | $P6_3/mmc$[56] | 326 | | 705 | 124 | | | | 198 | 248 |

elastic constant $C_{44}$ is related to the resistance to shear deformation and most important parameter that indirectly determines the hardness of solid indentation.[64] Second, it can be found that $C2/m$-$Ir_3B_2$ has the largest $C_{44}$, which is much larger than the theoretical values of $P_1$–IrB, α-$Ir_4B_5$, β-$Ir_4B_5$ and $P6_3/mmc$-$IrB_2$ synthesized experimentally, indicating that it exhibits higher hardness than the other iridium borides.

Materials with high bulk modulus usually have strong resistance to uniform compression. As shown in Table 3, the calculated bulk modulus ranges from 192 to 303 GPa, close to that of common hard materials such as $ZrB_2$ (220–245 GPa)[65] and $TiB_2$ (261 GPa),[63] but less than that of superhard materials $ReB_2$ (383 GPa),[9] and $WB_4$ (553 GPa),[12] indicating their strong ability to resist volume deformation. Among all the Ir–B compounds, $C2/m$-$Ir_3B_2$ and $Fmm2$-$Ir_4B_3$ have the highest bulk modulus (~300 GPa), which is larger than the theoretical values of $P_1$-IrB, α-$Ir_4B_5$, β-$Ir_4B_5$ and $P6_3/mmc$-$IrB_2$ reported by experiments, indicating that these two materials have the best incompressibility in Ir–B system. It is worth noting that some previous studies have shown that the bulk modulus may be directly related to the valence electron density (VED).[66] As for the iridium boride compounds, it appears that the general trend of the bulk modulus is consistent with that of VED (except for $P2_1/m$-$Ir_2B$) and the bulk modulus increases gradually with increasing VED.

Generally speaking, the larger value of the shear modulus also indicates that the orientation bonds between atoms are more obvious.[67] It is well known that the shear modulus of a material quantifies its resistance to shear deformation and is a more relevant predictor of material hardness than bulk modulus. The shear modulus of $C2/m$-$Ir_3B_2$ is 148 GPa, which is close to that of hard superconducting material NbN[68] (159.9 GPa) and larger than that of other Ir–B compounds. It is expected that $Ir_3B_2$ will resist shear strain to a large extent and has higher hardness than other Ir–B compounds.

Young's modulus, called the tensile modulus, is defined as the ratio of tensile stress to tensile strain in the elastic (linear) part of the stress–strain curve. When the value is large, the material is stiffer. The Young's modulus is also an important


© 2022 The Author(s). Published by the Royal Society of Chemistry

Table 3 The calculated the bulk modulus $B$ (GPa), shear modulus $G$ (GPa), Young's modulus $E$ (GPa), $B/G$, Poisson's ratio $\nu$, valence electron densities VED (e Å$^{-3}$), hardness $H_v^C$ (GPa), hardness $H_v^{MO}$ (GPa) and the fracture toughness $K$IC (MPa m$^{0.5}$) for the six considered structures in the Ir–B binary system

| Phase | Space group | $B$ | $G$ | $E$ | $B/G$ | $\nu$ | VED | $H_v^C$ | $H_v^{MO}$ | $K_{IC}$ |
|---|---|---|---|---|---|---|---|---|---|---|
| $Ir_2B$ | $P2_1/m$ | 255 | 96 | 256 | 2.66 | 0.33 | 0.563 | 6.2 | 14.0 | 3.66 |
| $Ir_3B_2$ | $C2/m$ | 301 | 148 | 381 | 2.04 | 0.29 | 0.552 | 13.1 | 19.4 | 5.67 |
| $Ir_3B_2$ | $C2/m$[22] | 302 | 150 | 386 | | | | | | |
| $Ir_4B_3$ | $Fmm2$ | 303 | 118 | 314 | 2.57 | 0.33 | 0.554 | 7.7 | 17.2 | 6.15 |
| $Ir_4B_3$ | $Fmm2$ (ref. 22) | 303 | 127 | 335 | | | | | | |
| IrB | $P2_1/m$ | 192 | 81 | 213 | 2.38 | 0.32 | 0.518 | 6.5 | 10.7 | 3.37 |
| $P_1$-IrB | $Pnma$[56] | 274 | 124 | 323 | 2.21 | | 0.540 | | | |
| $Ir_4B_5$ | $Cm$ | 274 | 112 | 297 | 2.44 | 0.32 | 0.539 | 10.6 | 17.1 | 5.18 |
| $Ir_4B_5$ | $Cm$[22] | 269 | 125 | 325 | | | | | | |
| $\alpha$-$Ir_4B_5$ | $C2/m$[58] | 225 | 63 | 180 | | 0.37 | | 4.5 | | |
| $\beta$-$Ir_4B_5$ | $Pnma$[58] | 265 | 99 | 266 | | 0.33 | | 8.5 | | |
| $Ir_3B_4$ | $Pnma$ | 290 | 120 | 316 | 2.42 | 0.32 | 0.537 | 8.7 | 17.0 | 5.78 |
| $IrB_2$ | $P6_3/mmc$[56] | 283 | 113 | 299 | 2.50 | | | | | |

parameter for measuring the stiffness of a material in addition to the bulk modulus and shear modulus. When the value is large, the material is stiffer. From Table 3, the Young's modulus (381 GPa) of $C2/m$-$Ir_3B_2$ is the highest, comparable to that of the well-known hard material ZrC,[69] indicating that $C2/m$-$Ir_3B_2$ has a higher hardness than the other Ir–B compounds. Poisson's ratio is an important parameter to describe the degree of directionality for the covalent bonding. Of all the phases considered, the $C2/m$-$Ir_3B_2$ has the smallest Poisson's ratio, which suggests that strong directional bonding exists in it and thus could be a potentially hard material. All of these excellent mechanical properties strongly suggest that $C2/m$-$Ir_3B_2$ is a potential candidate for hard material.

According to the standard of Pugh,[70] the toughness or brittle behavior of a solid can be estimated by the value of $B/G$. If $B/G >$ 1.75, the material shows toughness and *vice versa*, if $B/G <$ 1.75, the material shows brittleness. In the current situation, the $B/G$ values of several compounds are all higher than 1.75. Therefore, these six compounds exhibit toughness behavior.

The hardness of a material is an important parameter to evaluate the performance of a material, especially in industries such as cutting. As shown in Table 3, the $C2/m$-$Ir_3B_2$ has the highest hardness, regardless of the use of either Chen's model or Mazhnik-Oganov's model. It can be seen that the calculated theoretical hardness of the $C2/m$-$Ir_3B_2$ is 13.1 and 19.4 GPa based on Chen's model and Mazhnik-Oganov's model, which is close to that of commonly used hard materials like, for example, $RuB_2$[1] (15.1 GPa) or $Al_2O_3$[71] (17.8 GPa). It is consistent with result predicted from the elastic constant $C_{44}$, shear modulus and Young's modulus. The fracture toughness of $Fmm2$-$Ir_4B_3$, $Pnma$-$Ir_3B_4$ and $C2/m$-$Ir_3B_2$ are 6.15 MPa m0.5, 5.78 MPa m$^{0.5}$, and 5.67 MPa m$^{0.5}$, respectively, which is higher than that of WC[72] (5.37 MPa m$^{0.5}$). The results show that $Fmm2$-$Ir_4B_3$, $Pnma$-$Ir_3B_4$ and $C2/m$-$Ir_3B_2$ have strong resistance to fracture propagation.

### 3.3 Anisotropy properties

Elastic anisotropy is an important physical property of materials. It not only plays a vital role in technical and industrial applications, but also reflects the arrangement of atoms along the corresponding direction to a certain extent. The general elastic anisotropy index and the anisotropy percentage of crystals with any symmetry are defined as follows:[73]

$$A^U = 5\frac{G_V}{G_R} + \frac{B_V}{B_R} - 6 \geq 0 \quad (2)$$

$$A_1 = \frac{4C_{44}}{C_{11} + C_{33} - 2C_{13}} \quad (3)$$

$$A_2 = \frac{4C_{55}}{C_{22} + C_{33} - 2C_{23}} \quad (4)$$

$$A_3 = \frac{4C_{66}}{C_{11} + C_{22} - 2C_{12}} \quad (5)$$

For an isotropic solid, its $A^U$ is zero. The degree of anisotropy is shown by the deviation from zero. The greater the deviation from zero, the higher the degree of anisotropy of the material. In addition, the shear anisotropy constant can reflect the anisotropy of solids on different planes. For isotropic crystals, the values of $A_1$, $A_2$, and $A_3$ are equal to 1, and for any crystal less than or greater than 1, the degree of shear anisotropy of the crystal is indicated. Both the anisotropy index and the shear anisotropy factor are listed in Table 4.

Table 4 The calculated universal anisotropic index ($A^U$), shear anisotropic factors ($A_1$, $A_2$, and $A_3$) for the six considered structures in the Ir–B binary system

| Phase | Space group | $A^U$ | $A_1$ | $A_2$ | $A_3$ |
|---|---|---|---|---|---|
| $Ir_2B$ | $P2_1/m$ | 5.51 | 0.90 | 0.28 | 0.36 |
| $Ir_3B_2$ | $C2/m$ | 0.27 | 1.52 | 1.20 | 0.94 |
| $Ir_4B_3$ | $Fmm2$ | 0.45 | 0.57 | 0.79 | 0.66 |
| IrB | $P2_1/m$ | 3.60 | 2.88 | 1.59 | 1.23 |
| $Ir_4B_5$ | $Cm$ | 1.24 | 0.63 | 1.07 | 0.53 |
| $Ir_3B_4$ | $Pnma$ | 0.96 | 0.36 | 1.09 | 0.41 |

© 2022 The Author(s). Published by the Royal Society of Chemistry

For Ir–B compounds, the index $A^U$ order in Table 4 is $Ir_2B$ > IrB > $Ir_4B_5$ > $Ir_3B_4$ > $Ir_4B_3$ > $Ir_3B_2$. The results show that among Ir–B compounds, $Ir_2B$ has the highest elastic anisotropy, while $Ir_3B_2$ has the lowest elastic anisotropy. For the shear anisotropy constant, the values of the parameters $A_1$, $A_2$, and $A_3$ indicate that the anisotropy of Ir–B depends on the direction. $Ir_2B$ has the largest absolute values $(1 - A_2)$ and $(1 - A_3)$, while $Ir_3B_2$ and $Ir_4B_3$ have smaller absolute values. This indicates that Ir–B compounds have the strongest anisotropy on the (010) and (001) planes, while $Ir_3B_2$ and $Ir_4B_3$ have the opposite results. For the $Ir_2B$ compound, the value of $A_1$ is close to 1. This shows that $Ir_2B$ is isotropic along the (100) plane. In addition, $Ir_3B_2$ also exhibits isotropy on the (001) plane.

The three-dimensional surface model can more intuitively describe the anisotropic behavior of solid elasticity. The three-dimensional pattern of the reciprocal direction dependence of Young's modulus of the Ir–B compounds is different due to its different crystal structure. For different crystal structures of Ir–B compounds, there are different expressions for the constructing surfaces of Young's modulus.[74]

For monoclinic structure,

$$\begin{aligned}\frac{1}{E} = {} & l_1^4 S_{11} + 2l_1^2 l_2^2 S_{12} + 2l_1^2 l_3^2 S_{13} \\ & + 2l_1^3 l_3^2 S_{15} + l_4^2 S_{22} + 2l_2^2 l_3^2 S_{23} \\ & + 2l_1^2 l_2^2 S_{25} + l_3^4 S_{33} + 2l_1 l_3^3 S_{35} \\ & + l_2^2 l_3^2 S_{44} + 2l_1 l_2^2 l_3 S_{46} + l_1^2 l_3^2 S_{55} + l_1^2 l_2^2 S_{66}\end{aligned} \tag{6}$$

For orthorhombic structure,

$$\begin{aligned}\frac{1}{E} = {} & l_1^4 S_{11} + l_2^4 S_{22} + l_3^4 S_{33} \\ & + 2l_1^2 l_2^2 S_{12} + 2l_1^2 l_3^2 S_{13} + 2l_2^2 l_3^2 S_{23} \\ & + l_2^2 l_3^2 S_{44} + l_1^2 l_3^2 S_{55} + l_1^2 l_2^2 S_{66}\end{aligned} \tag{7}$$

*S*ijs are the elastic compliance constants and are shown in Table S2.† Fig. 4 displays the constructing surfaces for Young's modulus. The isotropic system will display a 3-dimensional sphere. The greater the deviation from the sphere, the higher the degree of anisotropy. In Fig. 4a, the 3D surface structure of $Ir_2B$ is longer along the *y* axis than other compounds, while the surface structure along the *x* and *z* axes is more compressed than other compounds. The results show that the monoclinic structure of $Ir_2B$ has the highest degree of anisotropy. In Fig. 4b, the 3D surface structure of the monoclinic $Ir_3B_2$ is closest to the sphere among all the structures, indicating that the anisotropy of $Ir_3B_2$ is the smallest. According to the three-dimensional surface structure, we can summarize the elastic anisotropy order of Ir–B compounds ($Ir_2B$ > IrB > $Ir_4B_5$ > $Ir_3B_4$ > $Ir_4B_3$ > $Ir_3B_2$). This order is consistent with the result obtained by the anisotropy constant $A^U$.

### 3.4 Electronic properties and chemical bonding

To further analyze the electronic properties of these Ir–B configurations, we calculated their electronic band structure and electronic density of states (DOS) (see Fig. S1† and 5). As

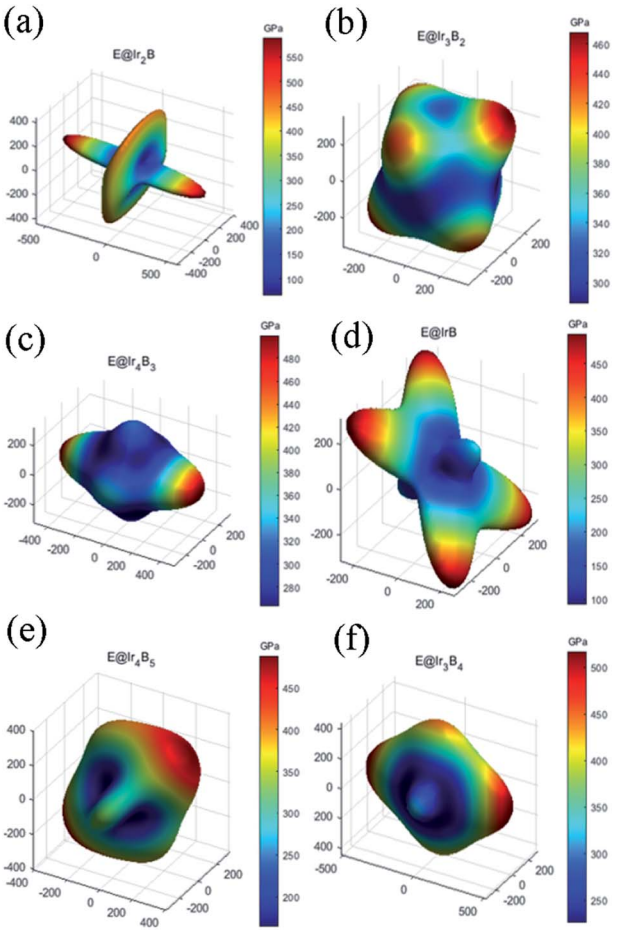


Fig. 4 Three-dimensional Young's modulus for (a) $P2_1/m$-$Ir_2B$, (b) $C2/m$-$Ir_3B_2$, (c) $Fmm2$-$Ir_4B_3$ (d) $P2_1/m$-IrB, (e) $Cm$-$Ir_4B_5$ and (f) $Pnma$-$Ir_3B_4$ under ambient pressure.

shown in the electronic band structure of Fig. S1,† these six phases have a strong overlap between the conduction band and the valence band, showing metallic characteristics. This can also be confirmed by the finite electron density of states of the Fermi level in Fig. 5. Moreover, in Fig. 5b and d–f, a typical feature in the TDOS can be seen that there is a deep valley at Fermi level for these compounds, that is, the presence of a so-called "pseudogap", which represents a borderline between the bonding and antibonding orbitals.[75] The presence of the pseudogap enhances the stability of the compounds.

To gain further insights into the chemical bonding nature in the six considered phases, we calculate the electron localization function (ELF), which can make a description of the bond type between atoms: large ELF values (>0.5) corresponds to the electrons of perfect covalent bonds or lone pairs, while smaller ELF values (<0.5) correspond to ionic or metallic bonds. As seen in Fig. 6, it is worth mentioning that these six crystals display a common feature of the ELF that the high electron localization can be seen between Ir and adjacent B atoms, implying the strong covalent bonding of Ir–B. Besides, from Fig. 6e and f, we can also clearly see high electron localization in regions between adjacent B atoms, which indicated the high covalence


© 2022 The Author(s). Published by the Royal Society of Chemistry

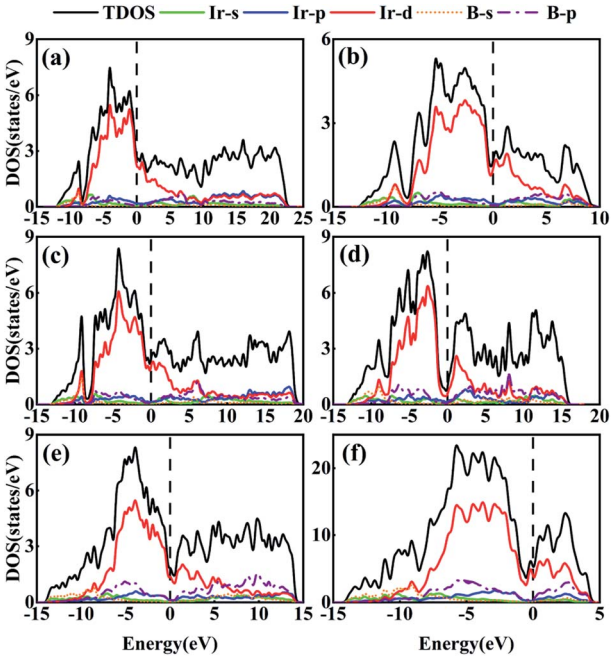


Fig. 5 Calculated electronic density of states for (a) $P2_1/m$-$Ir_2B$, (b) $C2/m$-$Ir_3B_2$, (c) $Fmm2$-$Ir_4B_3$ (d) $P2_1/m$-IrB, (e) $Cm$-$Ir_4B_5$ and (f) $Pnma$-$Ir_3B_4$ under atmospheric pressure.

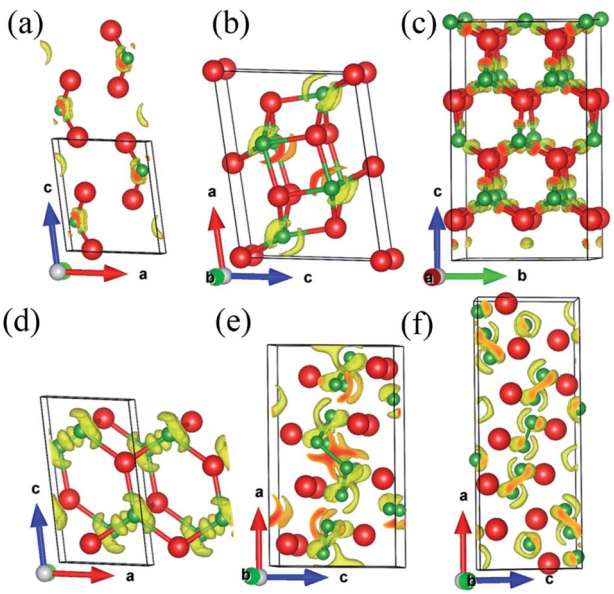


Fig. 6 ELFs of the (a) $P2_1/m$-$Ir_2B$, (b) $C2/m$-$Ir_3B_2$, (c) $Fmm2$-$Ir_4B_3$ (d) $P2_1/m$-IrB, (e) $Cm$-$Ir_4B_5$ and (f) $Pnma$-$Ir_3B_4$ (isovalue = 0.65).

of B–B bonding. According to the periodic law, the electronegativity value of the boron element (2.00) is less than the electronegativity value of the iridium element (2.2), which means that the charge should be transferred from the B atom to the Ir atom. Therefore, to analyze the actual charge distribution between B and Ir atoms, we explicitly measure the Bader charges of the B and Ir atoms for all six crystals, as summarized in Table 5. The average of transferred electrons charges from B

Table 5 Calculated Bader charges of Ir and B atoms in six considered phases. $\delta$ denotes the amount of charge transferred from B atom to the Ir atom

| Phase | Space group | Atom | Charge value ($e$) | $\delta$ ($e$) |
|---|---|---|---|---|
| $Ir_2B$ | $P2_1/m$ | Ir | 9.15 | −0.15 |
| | | B | 2.70 | 0.30 |
| $Ir_3B_2$ | $C2/m$ | Ir | 9.15 | −0.15 |
| | | B | 2.78 | 0.22 |
| $Ir_4B_3$ | $Fmm2$ | Ir | 9.17 | −0.17 |
| | | B | 2.77 | 0.23 |
| IrB | $P2_1/m$ | Ir | 9.41 | −0.41 |
| | | B | 2.59 | 0.41 |
| $Ir_4B_5$ | $Cm$ | Ir | 9.35 | −0.35 |
| | | B | 2.72 | 0.28 |
| $Ir_3B_4$ | $Pnma$ | Ir | 9.33 | −0.33 |
| | | B | 2.75 | 0.25 |

to the Ir atoms are about 0.3 $e$, 0.22 $e$, 0.23 $e$, 0.41 $e$, 0.28 $e$, 0.25 $e$ for $P2_1/m$-$Ir_2B$, $C2/m$-$Ir_3B_2$, $Fmm2$-$Ir_4B_3$, $P2_1/m$-IrB, $Cm$-$Ir_4B_5$, and $Pnma$-$Ir_3B_4$. Therefore, there is a small amount of charge transfer from B to the Ir atoms, indicating a covalent bonding character.

Finally, we calculated their integrated-crystal orbital Hamilton populations (ICOHPs) to depict the strength of chemical bonds in the six Ir–B phases by counting the energy-weighted population of wave function between two atomic orbitals (see Table S3†). The calculated ICOHP values ($\geq -2.28$ eV) of Ir–B in the six iridium borides are similar to those of B–B bonds in solid $\alpha$-B (2.00 Å, −3.49 eV), suggesting that Ir and B form covalent bonds. In addition, for the predicted $Cm$-$Ir_4B_5$ and $Pnma$-$Ir_3B_4$ compounds, the partial bonding states of B–B bonds shown in ICOHP are close to those in solid $\alpha$-B (2.00 Å, −3.49 eV) and even larger than those in solid $\alpha$-B (2.00 Å, −3.49 eV). In particular, in $Cm$-$Ir_4B_5$, it is also found that the shortest B–B pairs (1.89 Å) with the ICOHP value of −5.03 eV in graphene-like B sheet is only less than the ICOHP value of −7.72 eV in the smallest distance (1.67 Å) in $\alpha$-B, which indicates that there is the strongest B–B covalent interaction. This conclusion also demonstrates the validity of the analyses of the Ir–B bond length, ELF, and Bader charge. In other words, the DOS, ELF, Bader charge analyses, and ICOHP all suggest that six phases possess Ir–B covalent bonds. In addition, there are strong B–B interactions in $Cm$-$Ir_4B_5$ and $Pnma$-$Ir_3B_4$.

## 4 Conclusions

In a word, the lowest energy (or ground state) and low energy metastable structures of various stoichiometric Ir–B compounds have been systematically studied based on particle swarm optimization combined with first-principles calculation. Besides the three known theoretical structures, $C2/m$-$Ir_3B_2$, $Fmm2$-$Ir_4B_3$, and $Cm$-$Ir_4B_5$, we predicted three low-energy metastable phases for each of the three compounds, namely, $P2_1/m$-$Ir_2B$, $P2_1/m$-IrB, and $Pnma$-$Ir_3B_4$, respectively. The obtained phonon spectra and elastic constants confirm that all the predicted $P2_1/m$-$Ir_2B$, $C2/m$-$Ir_3B_2$, $Fmm2$-$Ir_4B_3$, $P2_1/m$-IrB, $Cm$-

© 2022 The Author(s). Published by the Royal Society of Chemistry

$Ir_4B_5$, and *Pnma*-$Ir_3B_4$ compounds are dynamically and mechanically stable. Six phases (except $P2_1/m$-IrB) have high bulk modulus and $B/G$ ratio, making them promising low compressible material and toughness material. In particular, $C2/m$-$Ir_3B_2$ has the highest Vickers hardness of 13.1 and 19.4 GPa based on Chen's model and Mazhnik-Oganov's model, which is a potential hard material. According to the general anisotropy index and three-dimensional surface structure, the elastic anisotropy order of borides is $Ir_2B$ > IrB > $Ir_4B_5$ > $Ir_3B_4$ > $Ir_4B_3$ > $Ir_3B_2$. Additionally, the calculated electronic band structure and density of states show that all Ir–B crystals studied exhibit electronic characteristics of metals. Further analysis on the computed density of states, electron localized function, Bader charge analyses, and ICOHP indicate that strong Ir–B covalent bonds are present in $P2_1/m$-$Ir_2B$, $C2/m$-$Ir_3B_2$, $P2_1/m$-IrB, and *Fmm*2-$Ir_4B_3$, while there are complex combinations of strong B–B and Ir–B covalent bonds in *Cm*-$Ir_4B_5$ and *Pnma*-$Ir_3B_4$. We hope that this comprehensive structure search can promote further experimental on the iridium borides.

## Author contributions

Jinquan Zhang: writing-original draft, visualization, formal analysis, software, investigation. Yuanyuan Jin: conceptualization, writing-review & editing, supervision, funding acquisition. Chuanzhao Zhang: conceptualization, software, writing-review & editing, data curation, supervision, funding acquisition. Yanqi Wang: validation, software. Libiao Tang: validation, software. Song Li: formal analysis, supervision. Meng Ju: funding acquisition, supervision. Jingjing Wang: software, supervision. Weiguo Sun: conceptualization, supervision. Xilong Dou: software, supervision.

## Conflicts of interest

Authors declare no conflicts to interest.

## Acknowledgements

This work was supported by the National Natural Science Foundation of China (No. 11804031, 11904297 and 11747139), the Scientific Research Project of Education Department of Hubei Province (No. Q20191301) and Talent and High Level Thesis Development Fund of Department of Physics and Optoelectronic Engineering of Yangtze University (C. Z. Z.).

## Notes and references

1 Q. Gu, G. Krauss and W. Steurer, *Adv. Mater.*, 2008, **20**, 3620–3626.
2 Y. Pan and Y. Lin, *Int. J. Quantum Chem.*, 2020, **120**, e26217.
3 Y. Pan and B. Zhou, *Ceram. Int.*, 2017, **43**, 8763–8768.
4 G. Akopov, M. T. Yeung and R. B. Kaner, *Adv. Mater.*, 2017, **29**, 1604506.
5 Y. Pan and S. Chen, *Vacuum*, 2022, **198**, 110981.
6 D. Pu and Y. Pan, *Vacuum*, 2022, **196**, 110727.
7 Y. Pan, *Chem. Phys. Lett.*, 2021, **783**, 139043.
8 Y. Pan and D. Pu, *Ceram. Int.*, 2020, **46**, 6698–6702.
9 H. Y. Chung, M. B. Weinberger, J. B. Levine, A. Kavner, J. M. Yang, S. H. Tolbert and R. B. Kaner, *Science*, 2007, **316**, 436–439.
10 A. šimůnek, *Phys. Rev. B: Condens. Matter Mater. Phys.*, 2007, **75**, 172108.
11 H. Niu, J. Wang, X. Q. Chen, D. Li, Y. Li, P. Lazar, R. Podloucky and A. N. Kolmogorov, *Phys. Rev. B: Condens. Matter Mater. Phys.*, 2012, **85**, 144116.
12 R. Mohammadi, A. T. Lech, M. Xie, B. E. Weaver, M. T. Yeung, S. H. Tolbert and R. B. Kaner, *Proc. Natl. Acad. Sci. U. S. A.*, 2011, **108**, 10958–10962.
13 H. Gou, A. A. Tsirlin, E. Bykova, A. M. Abakumov, G. Van Tendeloo, A. Richter, S. V. Ovsyannikov, A. V. Kurnosov, D. M. Trots, Z. Konôpková, H. P. Liermann, L. Dubrovinsky and N. Dubrovinskaia, *Phys. Rev. B: Condens. Matter Mater. Phys.*, 2014, **89**, 064108.
14 C. Lu and C. Chen, *J. Phys. Chem. Lett.*, 2021, **12**, 2848–2853.
15 C. Lu, W. Gong, Q. Li and C. Chen, *J. Phys. Chem. Lett.*, 2020, **11**, 9165–9170.
16 A. G. Kvashnin, D. V. Rybkovskiy, V. P. Filonenko, V. I. Bugakov, I. P. Zibrov, V. V. Brazhkin, A. R. Oganov, A. A. Osiptsov and A. Y. Zakirov, *Adv. Sci.*, 2020, **7**, 2000775.
17 A. G. Kvashnin, A. R. Oganov, A. I. Samtsevich and Z. Allahyari, *J. Phys. Chem. Lett.*, 2017, **8**, 755–764.
18 C. Zhao, Y. Duan, J. Gao, W. Liu, H. Dong, H. Dong, D. Zhang and A. R. Oganov, *Phys. Chem. Chem. Phys.*, 2018, **20**, 24665–24670.
19 A. R. Oganov, C. J. Pickard, Q. Zhu and R. J. Needs, *Nat. Rev. Mater.*, 2019, **4**, 331–348.
20 A. N. Kolmogorov, S. Shah, E. R. Margine, A. F. Bialon, T. Hammerschmidt and R. Drautz, *Phys. Rev. Lett.*, 2010, **105**, 217003.
21 L. P. Ding, Y. H. Tiandong, P. Shao, Y. Tang, Z. L. Zhao and H. Lu, *J. Phys. Chem. Lett.*, 2021, **12**, 5423–5429.
22 I. Zeiringer, X. Cheng, X. Q. Chen, E. Bauer, G. Giester and P. F. Rogl, *Sci. China Mater.*, 2015, **58**, 649–668.
23 Y. Wang, L. Wu, Y. Lin, Q. Hu, Z. Li, H. Liu, Y. Zhang, H. Gou, Y. Yao, J. Zhang, F. Gao and H. k. Mao, *Phys. Rev. B: Condens. Matter Mater. Phys.*, 2015, **92**, 174106.
24 A. G. Kvashnin, H. A. Zakaryan, C. Zhao, Y. Duan, Y. A. Kvashnina, C. Xie, H. Dong and A. R. Oganov, *J. Phys. Chem. Lett.*, 2018, **9**, 3470–3477.
25 D. V. Rybkovskiy, A. G. Kvashnin, Y. A. Kvashnina and A. R. Oganov, *J. Phys. Chem. Lett.*, 2020, **11**, 2393–2401.
26 H. Gou, N. Dubrovinskaia, E. Bykova, A. A. Tsirlin, D. Kasinathan, W. Schnelle, A. Richter, M. Merlini, M. Hanfland, A. M. Abakumov, D. Batuk, G. Van Tendeloo, Y. Nakajima, A. N. Kolmogorov and L. Dubrovinsky, *Phys. Rev. Lett.*, 2013, **111**, 157002.
27 J. Rau and A. Latini, *Chem. Mater.*, 2009, **21**, 1407–1409.
28 A. Latini, J. V. Rau, R. Teghil, A. Generosi and V. R. Albertini, *ACS Appl. Mater. Interfaces*, 2010, **2**, 581–587.
29 Z. Xie, R. G. Blair, N. Orlovskaya, D. A. Cullen, S. H. Lapidus, D. Kata, P. Rutkowski and J. Lis, *J. Solid State Chem.*, 2016, **233**, 108–119.


© 2022 The Author(s). Published by the Royal Society of Chemistry

30 Z. Xie, A. C. Terracciano, D. A. Cullen, R. G. Blair and N. Orlovskaya, *Adv. Appl. Ceram.*, 2015, **114**, 429–435.
31 Y. Wang, J. Lv, L. Zhu and Y. Ma, *Comput. Phys. Commun.*, 2012, **183**, 2063–2070.
32 Y. Wang, J. Lv, L. Zhu and Y. Ma, *Phys. Rev. B: Condens. Matter Mater. Phys.*, 2010, **82**, 7174–7182.
33 Y. Zhao, Y. Xu, P. Chen, Y. Yuan, Y. Qian and Q. Li, *Results Phys*, 2021, **26**, 104341.
34 W. Sun, X. Kuang, H. D. J. Keen, C. Lu and A. Hermann, *Phys. Rev. B: Condens. Matter Mater. Phys.*, 2020, **102**, 144524.
35 B. Chen, L. J. Conway, W. Sun, X. Kuang, C. Lu and A. Hermann, *Phys. Rev. B: Condens. Matter Mater. Phys.*, 2021, **103**, 035131.
36 W. Wang, C. Zhang, Y. Jin, S. Li, W. Zhang, P. Kong, C. Xie, C. Du, Q. Liu and C. Zhang, *Sci. Rep.*, 2020, **10**, 8868.
37 C. Zhang, G. Sun, J. Wang, C. Lu, Y. Jin, X. Kuang and A. Hermann, *ACS Appl. Mater. Interfaces*, 2017, **9**, 26169–26176.
38 G. Kresse and J. Furthmüller, *Phys. Rev. B: Condens. Matter Mater. Phys.*, 1996, **54**, 11169–11186.
39 J. P. Perdew, K. Burke and M. Ernzerhof, *Phys. Rev. Lett.*, 1996, **77**, 3865.
40 M. P. Teter, M. C. Payne and D. C. Allan, *Phys. Rev. B: Condens. Matter Mater. Phys.*, 1989, **40**, 12255–12263.
41 D. M. Bylander, L. Kleinman and S. Lee, *Phys. Rev. B: Condens. Matter Mater. Phys.*, 1990, **42**, 1394–1403.
42 H. Monkhorst and J. Pack, *Phys. Rev. B: Solid State*, 1976, **13**, 5188–5192.
43 W. Setyawan and S. Curtarolo, *Comput. Mater. Sci.*, 2010, **49**, 299–312.
44 A. Togo, F. Oba and I. Tanaka, *Phys. Rev. B: Condens. Matter Mater. Phys.*, 2008, **78**, 134106.
45 G. Henkelman, A. Arnaldsson and H. Jónsson, *Comput. Mater. Sci.*, 2006, **36**, 354–360.
46 W. Tang, E. Sanville and G. Henkelman, *J. Phys.: Condens. Matter*, 2009, **21**, 084204.
47 V. L. Deringer, A. L. Tchougreeff and R. Dronskowski, *J. Phys. Chem. A*, 2011, **115**, 5461–5466.
48 R. Hill, *Proc. Phys. Soc., London, Sect. A*, 1952, **65**, 349–354.
49 X. Q. Chen, H. Niu, D. Li and Y. Li, *Intermetallics*, 2011, **19**, 1275–1281.
50 E. Mazhnik and A. R. Oganov, *J. Appl. Phys.*, 2019, **126**, 125109.
51 M. Liao, Y. Liu, L. Min, Z. Lai, T. Han, D. Yang and J. Zhu, *Intermetallics*, 2018, **101**, 152–164.
52 D. H. Moseley, S. J. Thébaud, L. R. Lindsay, Y. Cheng, D. L. Abernathy, M. E. Manley and R. P. Hermann, *Phys. Rev. Mater.*, 2020, **4**, 113608.
53 A. R. Oganov, J. Chen, C. Gatti, Y. Ma, Y. Ma, C. W. Glass, Z. Liu, T. Yu, O. O. Kurakevych and V. L. Solozhenko, *Nature*, 2009, **457**, 863–867.
54 X. Li, H. Wang, J. Lv and Z. Liu, *Phys. Chem. Chem. Phys.*, 2016, **18**, 12569–12575.
55 B. Chu, D. Li, K. Bao, F. Tian, D. Duan, X. Sha, P. Hou, Y. Liu, H. Zhang, B. Liu and T. Cui, *RSC Adv.*, 2014, **4**, 63442–63446.
56 D. Y. Wang, B. Wang and Y. X. Wang, *J. Phys. Chem. C*, 2012, **116**, 1–21966.
57 S. Wei, D. Li, Y. Lv, Z. Liu, F. Tian, D. Duan, B. Liu and T. Cui, *J. Alloys Compd.*, 2016, **688**, 1101–1107.
58 B. Petermuller, C. Neun, K. Wurst, L. Bayarjargal, D. Zimmer, W. Morgenroth, M. Avalos-Borja, I. G. Becerril-arez, M. J. Muhlbauer, B. Winkler and H. Huppertz, *Inorg. Chem.*, 2018, **57**, 10341–10351.
59 D. Pu and Y. Pan, *J. Am. Ceram. Soc.*, 2021, **105**, 2858–2868.
60 E. Yu and Y. Pan, *Int. J. Hydrogen Energy*, 2021, **46**, 35342–35350.
61 D. Pu and Y. Pan, *Ceram. Int.*, 2022, **48**, 11518–11526.
62 D. Pu and Y. Pan, *Vacuum*, 2022, **199**, 110981.
63 P. Li, R. Zhou and X. C. Zeng, *ACS Appl. Mater. Interfaces*, 2015, **7**, 15607–15617.
64 B. Huang, Y. H. Duan, W. C. Hu, Y. Sun and S. Chen, *Ceram. Int.*, 2015, **41**, 6831–6843.
65 X. Zhang, X. Luo, J. Han, J. Li and W. Han, *Comput. Mater. Sci.*, 2008, **44**, 411–421.
66 R. B. Kaner, J. J. Gilman and S. H. Tolbert, *Science*, 2005, **308**, 1268–1269.
67 P. Ravindran, L. Fast, P. A. Korzhavyi, B. Johansson, J. Wills and O. Eriksson, *J. Appl. Phys.*, 1998, **84**, 4891–4904.
68 X. J. Chen, V. V. Struzhkin, Z. Wu, M. Somayazulu, J. Qian, S. Kung, A. N. Christensen, Y. Zhao, R. E. Cohen, H. k. Mao and R. J. Hemley, *Proc. Natl. Acad. Sci. U. S. A.*, 2005, **102**, 3198–3201.
69 D. Ferro, S. M. Barinov, J. V. Rau, A. Latini, R. Scandurra and B. Brunetti, *Surf. Coat. Technol.*, 2006, **200**, 4701–4707.
70 S. F. Pugh, *Philos. Mag.*, 1954, **45**, 823–843.
71 B. F. Levine, *J. Chem. Phys.*, 1973, **59**, 1463–1486.
72 S. G. Huang, K. Vanmeensel, O. Van der Biest and J. Vleugels, *Int. J. Refract. Hard Met.*, 2008, **26**, 41–47.
73 S. I. Ranganathan and M. Ostoja-Starzewski, *Phys. Rev. Lett.*, 2008, **101**, 055504.
74 Y. H. Duan, Y. Sun, M. J. Peng and S. G. Zhou, *J. Alloys Compd.*, 2014, **595**, 14–21.
75 P. Vajeeston, P. Ravindran, C. Ravi and R. Asokamani, *Phys. Rev. B: Condens. Matter Mater. Phys.*, 2001, **63**, 045115.

© 2022 The Author(s). Published by the Royal Society of Chemistry